RSC Advances

ROYAL SOCIETY OF CHEMISTRY

www.rsc.org/advances

Magnetic scaffolds of polycaprolactone with functionalized magnetite nanoparticles: Physicochemical, mechanical, and biological properties effective for bone regeneration

Jung-Ju Kim[a,b], Rajendra K. Singh[a,b], Seog-Jin Seo[a,b], Tae-Hyun Kim[a,b], Joong-Hyun Kim[a,b], Eun-Jung Lee[a,b], Hae-Won Kim[a,b,c,*]

[a] *Department of Nanobiomedical Science and BK21 PLUS NBM Global Research Center for Regenerative Medicine, Dankook University, Republic of Korea*

[b] *Institute of Tissue Regeneration Engineering (ITREN), Dankook University, Republic of Korea*

[c] *Department of Biomaterials Science, College of Dentistry, Dankook University, Republic of Korea*

---

* Corresponding author:

Prof. Hae-Won Kim: tel) +82 41 550 3081, fax) +82 41 550 3085, e-mail: kimhw@dku.edu

For: RSC Advances

Abstract

Magnetic scaffolds have gained significant attention for the disease treatment and tissue repair. Here we focus on magnetic nanocomposites scaffolds made of poly(caprolactone) (PCL) and magnetite nanoparticles (MNPs) for bone repair. The physico-chemical, mechanical, and magnetic properties of the scaffolds, the in vitro cell responses, and the in vivo tissue compatibility were examined in-depth to find the effectiveness for uses as bone scaffolds. The MNPs, produced by a surfactant-mediation process, were well-distributed within the PCL matrix to enable homogeneous nanocomposites. The PCL-MNP scaffolds showed excellent magnetic properties, preserving the superparamagnetic behavior. Incorporation of MNPs greatly improved the hydrophilicity and water swelling of scaffolds. Acellular apatite forming ability test revealed a higher mineral induction on the magnetic scaffolds than on the PCL scaffold. The mechanical stiffness increased significantly with the addition of MNPs, when tested under both static and dynamic compressed wet conditions. The initial cell adhesion to the magnetic scaffolds was substantially improved by ~1.4-fold with respect to the pure PCL scaffold, enabling earlier cellular proliferation confluence. The cell mineralization, as assessed by the quantification of calcium deposits, was significantly enhanced on the magnetic scaffolds. The magnetic scaffolds, subcutaneously implanted in rats for 2 weeks, revealed favorable tissue compatibility, with substantial fibroblastic cell invasion and neoblood vessel formation while exerting minimal inflammatory reactions. The results, demonstrating excellent physico-chemical, magnetic, mechanical and biological properties of the PCL-MNP scaffolds, support the potential use of the magnetic scaffolds for bone repair and regeneration.

Keywords: Bone scaffolds; Magnetic nanoparticles, Nanocomposites; Bone cell responses; Bone repair

1. Introduction

Magnetic nanoparticles (MNPs) have shown great promise in the biomedical fields due to their special physical properties, which include dimensions at the nanoscale and unique reaction to magnetic forces, providing favorable cell and tissue responses. Over the past decade, biomedical applications of MNPs have ranged from hyperthermia therapy to magnetic resonance imaging and even to magnetic drug delivery.[1, 2] In the meanwhile, very few studies have been reported on the use of MNPs as a scaffold for tissue engineering. Scaffolds, as the key component in tissue engineering, aid in the adhesion and spreading of cells, support their growth and subsequently trigger their development to specific tissues. Therefore, engineering a scaffold with properties to improve these cellular processes is the key issue in scaffold development for tissue engineering.

Recently, MNPs have been introduced as the nanocomponent that can be incorporated within polymeric scaffolds to provide additional magnetic properties to the scaffolds.[3-6] The incorporation of inorganic nanoparticles including MNPs is considered a promising strategy to produce biopolymer-based bone scaffolds with properties more suitable for bone repair and regeneration, in terms of mechanical and biological aspects.[7-9] In particular, the MNPs incorporated in the scaffolds are considered to play a number of important roles in the stimulation and alteration of cellular responses which are favorable for bone formation and disease treatments. Under magnetic fields, the magneto-mechanical induction of bone cells or the temperature-induced hyperthermia therapy of cancerous cells are the possible reasons that explain the usefulness of the scaffolds.[7, 8]

To this end, here we develop MNPs-incorporated magnetic biopolymer scaffolds for the purpose of bone repair. The surface-functionalized MNPs were added at small quantities to polycaprolactone (PCL) and a salt-leaching method was introduced to produce foam scaffolds. The physico-chemical, mechanical, and magnetic properties of the PCL-MNP scaffolds were investigated, and the bone cell responses as well as the tissue compatibility in rats were assessed to find further usefulness for bone tissue engineering.

2. Experimental procedures

2.1. Preparation of MNPs and PCL-MNP scaffolds

MNPs were synthesized using a method developed by Sun et al.[9] Briefly, MNPs (10 nm in diameter) were prepared by mixing 3.5318 g Fe(acac)$_3$ (iron(III) acetylacetonate), 3.9123 g 1,2-hexadecanediol, 10 ml of oleic acid, 10 ml of oleylamine, and 40 ml of benzyl ether under a flow of nitrogen gas. The mixture was preheated to reflux at 200 ºC for 30 min while stirring, and then heated to 300 ºC for an additional 2 h under a nitrogen atmosphere. The black-brown mixture was allowed to cool to room temperature and 50 ml of ethanol was added to the precipitate. The products were collected by centrifugation at 10,000 rpm for 5 min and then washed 4 times with ethanol and dried at 50 ºC. The morphology and magnetic properties of the MNPs were characterized using transmission electron microscopy (TEM, 7100 microscope, JEOL, USA) and a vibrating sample magnetometer (VSM, Quantum Design MPMS-XL7, USA).

For the preparation of PCL-MNP scaffolds, 10% w/v of PCL (~ 80 kDa, Sigma-Aldrich, USA) was first dissolved in chloroform, and the MNPs were then added to the PCL solution. The concentrations of MNPs in PCL solutions were prepared at 0, 5, and 10 wt%, which designated as the PCL, PCL-MNP5, and PCL-MNP10, respectively. The mixture solutions were ultrasonicated to ensure they were homogeneous and stable. The NaCl particles sieved (200-500 μm in diameter) were poured into a cylindrical plastic mould and then packed tightly by a manual pressing, after which the mixture solutions were poured dropwise into the NaCl-filled mold, and then followed by freezing at -70 ^{o}C and freeze-drying for 3 days. The resulting samples were washed with distilled water for 10 min (x 9) while agitating at 100 rpm to leach out the salt completely, and then dried again.

2.2. Characterizations of PCL-MNP scaffolds

Morphologies of the scaffolds were observed by scanning electron microscopy (SEM; S-3000H Hitachi, Japan), and the atomic composition was analyzed with energy dispersive spectroscopy (EDS). The phase of the scaffolds was characterized by X-ray diffraction (XRD; Rigaku, USA). The scaffolds were scanned in the range of diffraction angle 2θ = 10-60º at a rate of 2º min^{-1} with a step width of 0.02º, 2θ using Cu Kα1 radiation at 40 kV and 40 mA current strength. Fourier transformed infrared

(FT-IR; Perkin-Elmer, USA) spectroscopy was used to observe the chemical status of the scaffolds. Thermogravimetric analysis (TGA) was carried out to analyze the thermal behavior and compositional fraction of the scaffolds. The samples were heated from room temperature to 500 ºC at a heating ratio of 10 ºC/min under nitrogen atmosphere.

The capacity of the scaffolds to take up water[10] or ethanol[11] was measured by the weight change before and after the soaking tests, as follows: $\Delta W_S (\%) = ((W_S - W_0)/W_0) \times 100$, where W_0 and W_S are the scaffold weights before and after the soaking, respectively. The porosity and density of the scaffolds were measured using a mercury porosimeter (PM33, Quantachrome, USA). The specific surface area was analyzed by the Brunauer-Emmett-Teller (BET) method under nitrogen gas. The hydrophilicity of the scaffolds was investigated by measuring the water contact angle using a Phoenix300 analyzer. Water droplet images made on the scaffold surface were obtained using a viewing system until equilibrium was reached at 25 ^{o}C. Typical images of the water droplet at an equilibrium state were taken for each sample, and five samples were tested for each group.

The apatite forming ability of the scaffolds was investigated immersing in a concentrated SBF (2 x SBF), which was used to speed up the apatite induction process and thus to shorten the evaluation periods of the apatite forming ability of bioactive materials.[12] Each sample (5 mm in diameter and 3 mm in thickness) was contained in 10 ml of 2 x SBF and then incubated at 37 ºC for the given periods (1, 3, and 7 days). At each time, samples were collected, washed with distilled water, and dried at room temperature. Their apatite-forming abilities were analyzed using SEM and XRD.

The magnetic properties of the samples were measured by a VSM in an applied magnetic field of ± 20 kOe at room temperature[13], in terms of saturation magnetization and hysteresis loops. VSM was calibrated using a standard reference (high purity nickel sphere), supplied with the instrument.

2.3. Mechanical evaluation of scaffolds

The mechanical properties of the PCL-MNP scaffolds were measured by a dynamic mechanical analysis (DMA, DMA25N, MetraVib, USA) under static and dynamic compression in wet conditions, as reported elsewhere.[14] A cylindrical sample (8 mm in diameter and 16 mm in height) was first soaked completely with PBS for 1 day. For a static test, samples were measured at a constant compressive load while recording the strain with respect to time. Three different samples were tested at each condition, and obtained values were averaged.

Next, dynamic was performed on a parallel plate configuration. Mechanical spectrometry was monitored using dynamic frequency sweep with frequencies ranging from 0.5 to 10 Hz for 10 min at room temperature. The storage modulus (E') and loss modulus (E'') were recorded. The tangent delta was evaluated from the ratio of E''/E'.

2.4. In vitro cell adhesion, growth and mineralization tests

MC3T3-E1 cells (ATCC; American type culture collection) were cultured in α-Minimal Essential Medium (α-MEM, Gibco, USA) supplemented with 10% of fetal bovine serum (FBS, Hyclone, Thermo Scientific, USA), 100 U/mL of penicillin, and 100μl of streptomycin at 37 ℃ in a humidified atmosphere containing 5% of CO_2 for 7 days. 10^5 cells were seeded onto the scaffold (5 mm in diameter x 3 mm in height). After 1 day, the scaffold moved to each well of another plate, and the cell adhesion rate on the scaffold was measured by a cell counting kit (CCK). The cell proliferation was further assessed by the CCK method, for the culture periods of 3, 7, 14, and 21 days. For SEM observation of cells, samples were fixed in a solution of 2.5% glutaraldehyde, dehydrated in a gradient series of ethanol solutions, dried at room temperature, and coated with a thin layer of platinum.

The cellular mineralization was assessed by the Alizarin red assay (ARS; Sigma Aldrich, USA). After culturing for 14, 21 and 28 days, the cells were fixed with 70% ethanol for 1 h at 4 ℃, and then immersed in 2% w/v of aqueous ARS solution (pH 4.1~4.3) for 30 min at room temperature. After several washes with distilled water, these stained samples were removed and eluted with 10% w/v of cetyl pyridinium chloride (CPC) in 10 mM sodium phosphate (pH 7) for 1 h. The absorbance of eluents was then read using a micro-plate reader at 595 nm after normalization with the total amount of mitochondrial dehydrogenase in the cells for the consistent quantitative assay of each sample solution.

2.5. In vivo tissue compatibility test

The *in vivo* experiments were approved by Dankook University Institutional Animal Care and Use Committee, Korea. Three ten-week-old male Spraque-Dawley rats weighing 250-350 g were used. Experimental scaffold groups were PCL, PCL-MNP5, and PCL-MNP10, and four samples (5 mm in diameter x 3 mm in height) per group were implanted. Prior to implantation, the scaffolds were sterilized with ethylene oxide gas. The animals were anesthetized with an intramuscular injection of 80 mg/kg ketamine and 10 mg/kg xylazine of body weight. The skin on the dorsal region of the rat was shaved and asepsis of the operatory area was achieved with povidone and 70% ethanol. A 2 cm long linear incision was made in the skin using a # 10 blade mounted onto a bard-parker scalpel. Four small subcutaneous implant sites were made by blunt dissection with Halsted-mosquito hemostatic forceps on the back side in a lateral direction from the spine of each rat. Scaffolds were inserted into the prepared area, away from the incision point. The incision was subsequently sutured with 4-0 non-absorbable monofilament suture material (Dafilon®, B. Braun, Germany). During and after surgery, the rats were kept warm under observation until recovered from the anesthesia, after which the rats were housed, one rat per cage. The animals were kept on a 12 h light / 12 h dark schedule in the cages and provided with standard pellet food and water *ad libitum*.

Two weeks after the implantation, the animals were sacrificed by cervical dislocation. The tissue samples harvested for histologic analysis were immediately immersed in 4% buffered formaldehyde for 24 h at room temperature, and dehydrated in a series of graded ethanol. The specimens were bisected and embedded in paraffin. Paraffin blocks were serially sectioned at 5 μm thicknesses along the longitudinal axis using a rotary microtome. The slides were classically stained with hematoxylin and eosin (HE) or Masson's trichrome (MT) stain, and were then observed with a light microscope for biocompatibility and vessel formation. Histological scores, given the points indexing absent (1), mild (2), moderate (3), and severe (4) degrees, obtained from both stained slides included the extent of inflammatory response, thickness of fibrous capsule, presence of blood vessel, and proliferation of fibroblasts.

2.6. Statistical analysis

Data were presented as the mean ± one standard deviation. The statistical analysis was performed using a one-way ANOVA test by comparing between independent sample groups. Significance was considered at $p < 0.05$ or $p < 0.01$.

3. Results and discussion

3.1. Characteristics of PCL-MNP scaffolds

As the magnetic nanocomponent, we prepared surface-functionalized magnetite (Fe_3O_4) nanoparticles. Magnetite is well-known as a class of magnetic iron oxide materials that has a cubic crystal form[15] and the nanoparticle form tends to agglomerate in the aqueous environment owing to the short-range van der Waals forces.[16] Therefore, the improvement of dispersibility in aqueous media has been one of the key issues in the development of MNPs. Our surface-functionalized MNPs were prepared by the reaction of $Fe(acac)_3$ with surfactants such as alcohols, oleic acids, and oleylamine at high temperature.[17] From a typical TEM micrograph (**Fig. 1a)**, spherical and well-dispersed MNPs were observed with a narrow size distribution (an average size of 10.7 nm). The magnetic hysteresis curve of the as-synthesized MNPs measured by VSM at room temperature is shown in **Fig. 1b**. The MNPs have a saturation magnetization of 72.1 emu g^{-1}. The VSM curve passed through the zero point, and remnant magnetization and coercivity were not observed in the VSM curve, indicating that the superparamagnetism of the MNPs was preserved at room temperature. This is very consistent with the previous results.[9, 18, 19]

The surface-functionalized MNPs were then incorporated within the PCL scaffolds at different contents. The surface-functionalized MNPs were well dispersed in the chloroform solution, which was used to dissolve PCL. The porous scaffold of PCL-MNP scaffolds was then achieved via a salt leaching technique. The pore structure properties such as pore size, pore distribution, and porosity can affect the physicochemical properties of the porous scaffolds and the cellular behaviors.[20-22] **Fig. 2** shows SEM micrographs and EDS mapping images of the scaffolds on a cross-sectional view. All the scaffolds showed a well-developed pore structure without significant difference in the pore morphology. The macropores larger than 250 μm are known to be suitable for cell penetration and engraftment whilst those smaller than 100 μm restrict cellular infiltration within the pores.[23] According to the reports on the effects of pore size on osteoblast activity, pores larger than 300 μm were preferred for the induction of osteogenesis.[23] Therefore, the pores ranging from 250 to 500 μm implemented in this study will be suitable for bone tissue engineering applications. The EDS mapping revealed higher Fe signals in the MNP-incorporated scaffolds, and the signal distribution was observed to be uniform.

The porosity of the scaffolds, first estimated using the ethanol replacement test, was shown to be 65~70 %, which was in similar range to the porosity measured by the mercury intrusion porosimetry. Other properties such as bulk density and skeletal density could also be obtained by this method,[24, 25] as summarized in **Table 1**. While the porosity was similar among the scaffolds, the density level increased with increasing MNP content, which was due to the higher density of inorganic MNPs than PCL. The surface area of the scaffolds, measured by BET analysis, was shown to increase with increasing MNPs. Of note, the surface area of scaffolds was not dependent on porosity; rather, the value increased with increasing the MNPs content, which might be interpreted that the MNPs evenly embedded within the PCL polymeric matrix, with their nano-sized characteristic, should improve the surface area of the scaffolds.

The physico-chemical properties of the PCL-MNP scaffolds were further confirmed. The phase of the scaffolds was examined by XRD analysis (**Fig. 3a**). The MNPs showed diffraction peaks at $2\theta \approx 31°, 36°, 43°, 54°, 57°$, and $63°$, typical of bulk magnetite Fe_3O_4.[26] The average particle size, as calculated by Scherrer equation[27] for the strongest diffraction peak (311), was 10.7 ± 0.019 nm, close to the size determined by TEM image. The magnetite peaks of the PCL-MNP scaffolds were more clearly observed with an increase in MNPs. The chemical bond structure of the scaffolds, as revealed by the FT-IR spectrum (**Fig. 3b**), showed typical bands related to PCL and MNPs, including a distinctive band at 578 cm^{-1} assigned to the Fe-O bond vibration of MNPs.[28, 29] This band became sharper in the PCL-MNP scaffolds with an increase in MNP content. Typical PCL vibration bands of C=O and C-O stretching were observed at 1720 and 1293 cm^{-1}, respectively. In addition, a weak and broad O-H stretching band of PCL was assigned to alcohol groups at 3153-3640 cm^{-1}. The thermal behavior of the scaffolds was monitored by TGA (**Fig. 3c).** The TGA curve of pure MNP showed a certain level of weight loss (~10%), which was presumably due to the residual organic phases. While a typical thermal decomposition of the pure PCL was shown at almost 400 ^{o}C (99% loss), the PCL-MNP scaffolds left certain levels of weight, which was ascribed to the presence of the MNP component in the scaffolds. Taking the weight losses of pure MNP and PCL also into consideration, the contents of MNPs within the PCL-MNP5 and PCL-MNP10 scaffolds were approximately 4.71 and 10.01 wt.%, respectively, which was nearly consistent with the contents of MNPs incorporated in the preparation of the scaffolds.

3.2. Water affinity, swelling, and apatite forming ability of scaffolds

Water affinity results of the scaffolds are shown in **Fig. 4**. While the pure PCL scaffold showed a high degree of hydrophobicity (contact angle of as high as 85°), the PCL-MNP scaffolds became more hydrophilic (61° for 5% and 47° for 10% MNP) as shown in **Fig. 4a**. This was due to the existence of MNPs, more specifically, the carboxyl groups present on the surface of MNPs. In fact, during the salt leaching process, the surface of MNPs is possibly carboxylated. Jadhav et al. suggested that oleic acid, used as a surfactant to cap MNPs, electrostatically interacts with salt ions, resulting in dissociation of the COOH groups of oleic acid into COO^- and H^+, and consequently improving the hydrophilicity of MNPs.[30] We also found that the water dispersibility of the surfactant-capped MNPs markedly increased after the treatment with sodium chloride solution (data not shown).

As a result of this enhanced hydrophilicity, the PCL-MNP scaffolds showed an excellent water uptake capacity. The water uptake, measured for a period of up to 24 h, showed a significant difference between samples (**Fig. 4b).** The water uptake of PCL-MNP scaffolds quickly occurred within a few hours to reach almost saturation levels. The water uptake increased with increasing MNP content. As a result, after 24 h, the water uptake was recorded as ~1440% for PCL, 1870% for PCL-MNP5, and 2850% for PCL-MNP10 scaffolds. The water uptake capacity of the PCL-MNP10 scaffold was almost two-fold higher than that of the pure PCL scaffold. Furthermore, the scaffolds were observed to swell apparently after the water uptake. The increased volume of scaffolds, as optically measured (**Fig. 4c)**, was in the order: 5 % in PCL < 8 % in PCL-MNP5 < 11 % PCL-MNP10, signifying a two-fold increase with 10% MNP addition to PCL. In fact, the water uptake level was due to both the pore-filling of water and the swelling of scaffolds. When considering the similar porosity levels for all scaffolds, the difference in water uptake capacity was primarily a result of the swollen (dimension-changed) property, i.e., swelling a scaffold through taking-up water molecules within the MNP-dispersed hydrophilic polymeric network should reflect the substantially increased water uptake behavior of the magnetic scaffolds.

The *in vitro* acellular mineralization behavior of PCL-MNP scaffolds was evaluated after immersion in SBF. **Fig. 5** shows the SEM morphologies and XRD patterns of the scaffolds after the SBF-immersion. The PCL-MNP5 and PCL-MNP10 scaffolds began to form mineral nanocrystallites on the surface as early as day 1, and the mineral phase covered the entire surface at day 3. After 7 days, the mineral crystallites had grown substantially (**Fig. 5a**). On the other hand, the pure PCL scaffold started to show mineral formation at day 3, and then surface coverage at day 7 with much smaller crystals than those observed in the PCL-MNP scaffolds. The XRD patterns strongly supported the SEM results based on the characteristic peaks of HA crystal ($2\theta \approx 26^\circ$ and 32°) (**Fig. 5b**). It was thus clear that the MNP-incorporation enhanced the mineralization behavior of the scaffolds in SBF. This is due primarily to the surface-carboxylated MNPs distributed within the scaffolds. The calcium ions in the medium would be better attracted to the negatively-charged scaffold surface, and subsequently attract the phosphate ions to form mineral nuclei for crystallization.[31, 32] While the information on this behavior in SBF is somewhat limited because no cells were engaged in and the condition was not dynamic, the acellular mineralization results enable forecasting of the possible surface reactions and bone bioactivity of the magnetic scaffolds useful for bone regeneration purpose. As the biological properties of the scaffolds we also assessed the cell and tissue compatibility.

3.3. Magnetic and mechanical properties of scaffolds

MNPs produce a magnetic field surrounding the tissue following implantation, providing the matrix scaffolds physical conditions possibly beneficial for the native cell and tissue microenvironments.[33] For instance, the recent idea to utilize magnetic scaffolds in tissue engineering has been suggested for an alternative mediation of the angiogenesis process *in vivo*.[34] Here we examined the magnetization of the produced PCL-MNP magnetic scaffolds. The magnetic force of the PCL-MNP scaffolds will be dominated by the MNPs dispersed in the matrix. Magnetic properties of dry PCL-MNP scaffolds at room temperature were characterized from their typical hysteresis curves measured by VSM. **Fig. 6a** shows the magnetization *versus* magnetic field curves of PCL-MNP scaffolds. The hysteresis loops of PCL-MNP scaffolds showed a similar tendency to that of MNPs, and the magnetization value of PCL-MNP scaffolds was linearly proportionate to the MNP content (1.6 and 3.1 emu g^{-1}, respectively, with 5% and 10% MNP content). Similarly to the hysteresis loop of pure MNPs, coercivity and remanence were not observed in the curves of the PCL-MNP5 and PCL-MNP10 scaffolds, which indicates the superparamagnetism of the scaffolds.[35] Field-dependent magnetic moments were nearly linear up to 0.5 kOe, reaching around 80% of the saturation magnetization value, which is obtained when materials can maximally reach the magnetization under the sufficient magnetic field.[36] Therefore, maximal magnetizations could be easily achieved in the magnetic scaffolds with only a small change in the external magnetic field. **Fig. 6b** shows the magnetic interaction of the scaffolds by measuring distances between a permanent magnet and a magnetized scaffold.[37] The distance for pure PCL scaffolds was zero, while distances for magnetized PCL-MNP5 and PCL-MNP10 scaffolds were 4.43 and 7.23 mm, respectively, which indicates the external magnetic field-guided distances of the magnetized scaffolds. Additive images show the magnet-attached scaffolds. Based on the magnetic properties, the PCL-MNP scaffolds were considered to preserve the superparamagnetic behavior of incorporated MNPs, although the saturation magnetization in the magnetic scaffolds was relatively small due to the small concentrations of MNPs. Further studies warrant the elucidation of the *in vivo* efficacy of the magnetic scaffolds in stimulating tissue repair or disease treatment through the *in situ* generated magnetism effects.

The mechanical behaviors of the PCL-MNP scaffolds were also examined under static and dynamic conditions using wet samples, as shown in **Figs. 7** and **8**, respectively. The mechanical properties are another important consideration of scaffolds targeting for bone repair and regeneration. **Fig. 7a** shows the typical stress-strain curves of the scaffolds under a static compressive load. All three scaffolds exhibit similar behavior. The stress value continues to increase with increasing strain, and the stress increasing rate increases during compression, which is generally observed in the porous materials in the course of densification and pore collapse under a compressive load. The incorporation of MNPs in the scaffolds recorded increased stress levels over the entire strain range, indicating higher resistance to deformation under a compressive load. The inset shows an initial linear region of stress-strain curves (within 2% strain), and the elastic modulus was obtained from the initial linear slope (**Fig. 7b).** The elastic modulus of PCL, PCL-MNP5, and PCL-MNP10 was 1.2, 1.4, and 2.4 MPa, respectively, demonstrating that the MNPs distributed in the matrix played a significant role in stiffening the scaffolds.

Along with the static mechanical test, a dynamic mechanical analysis was further over a frequency range from 1 to 10 Hz performed under a constant strain.[38] The storage modulus (*E'*; indicating the material elastic response to stress), loss modulus (*E"*; indicating the material viscous response to stress),[39] and tangent delta (*E"/E'*) were recorded, as shown in **Fig. 8**. The scaffolds exhibited little frequency-dependence for all the properties. The E' values were much higher than the E'' values, by four orders of magnitude, indicating that the PCL-MNP scaffolds have the ability to store elastic energy without a significant loss of polymeric viscosity. Importantly, the increase in MNP content significantly increased the storage modulus of the scaffolds, a coherent result of the static test.

There was little difference in the tangent delta among the scaffolds, as both storage and loss moduli increased similarly with MNPs incorporation. It is considered that the improved hydrophilicity and thus higher swelling of scaffolds, due to the MNP-incorporation, results in such change in modulus values. Although the MNPs themselves would render the PCL polymer network much stiffer, the increased volume (thus distance between polymer chains) in water and the interspaced water molecules should compensate the rigidity.

3.4. In vitro osteoblastic responses to magnetic scaffolds

The *in vitro* cell responses to the magnetic scaffolds were first assessed by the cell adhesion. **Fig. 9a** shows SEM micrographs of cell-attached PCL and PCL-MNP scaffolds performed at 1, 3, and 24 h after cell seeding. Granule-like MC3T3-E1 cells were well revealed on the PCL-MNP5 and PCL-MNP10 scaffolds at 3 h after cell seeding, and the cells were found more abundantly in those nanocomposite scaffolds than those on the pure PCL scaffold. In order to quantify the cell adhesion level, CCK measurement was conducted, as shown in **Fig. 9b**. There was no significant difference of time-dependent cell adhesion rate in the pure PCL scaffold. On the contrary, in the PCL-MNP5 and PCL-MNP10 scaffolds, cell adhesion rapidly increased at 3 h after cell seeding and thereafter slightly increased up to 24 h. At 3 h, the cell adhesion level on the PCL-MNP10 scaffold was approximately 1.4-fold higher than that on pure PCL scaffold.

The cell morphology, proliferation, and differentiation *in vitro* were further investigated. **Fig. 10a** shows SEM micrographs of cells grown on the scaffolds for 14 days. All the scaffolds were highly populated with cells showing a number of cells and cellular products revealed throughout the scaffolds. There appeared to be little difference in the cell grown morphologies among the scaffolds. The proliferation of cells cultured on the scaffolds was then monitored for up to 21 days, as shown in **Fig. 10b**. Cells grew rapidly up to 14 days for all scaffolds. Long-term cultures of cells over 14 to 21 days did not increase the cellular population, which was considered to be related to the confluence of cells on the scaffold surface and/or to the switch of the cellular proliferative potential dominantly into a differentiation. Interestingly, the cell proliferation rate, particularly after 7 days, was higher on the pure PCL scaffold than on the PCL-MNP scaffolds, with significant differences noticed at days 14 and 21 (1.3~1.5-fold difference). It is thus considered that the cell proliferation rate from day 7 to 14 was higher on pure PCL. It is presumed that the cells on the PCL-MNP scaffolds might experience more rapid proliferation-to-differentiation switch to undergo more active osteogenic differentiation processes.

As the final stage of osteogenic differentiation, the cellular mineralization is always considered and is of special importance. We analyzed the cellular mineralization behavior on the scaffolds by means of quantification of calcium deposits. For this, the staining of ARS that selectively binds to calcium was performed.[40] **Fig. 11a** shows the ARS quantified calcium deposit level on the cells cultured on each scaffold. While little difference was shown among scaffolds at days 7 and 14, a significant difference was noticed at day 21, which was a relatively prolonged culture period. The calcium level on the PCL-MNP10 scaffold was approximately 2.8-fold higher than that on the pure PCL scaffold. The mineral deposits in the PCL-MNP10 scaffold at day 21 were analyzed by EDS (**Figs. 11b**). The EDS mapping revealed high signals of Ca (in green) and P (in blue) with a Ca/P ratio of 1.7, being similar to that of stoichiometric HA. From these results, it is also evident that the cell mineralization was significantly enhanced on the magnetic scaffolds, indicating that the surface-functionalized MNPs in the scaffolds helped cellular osteogenesis and the final stage of mineralization. Although here we assessed the final stage of osteogenesis, more in-depth investigation into osteogenic behaviors including osteogenic gene expressions and protein syntheses will be warranted as further studies to elucidate the improved cellular mineralization. It is considered that the cells entering into an osteogenic differentiation could produce sufficient levels of bone matrix proteins, which are critically involved in subsequent cellular mineralization.

At this point, the reason for the improvement of cellular proliferation and osteogenic differentiation by the magnetic scaffolds needs to be discussed. The significant improvement in cell adhesion on the PCL-MNP magnetic scaffolds may first be attributed in part to the hydrophilic nature of the scaffolds that improves the affinity of proteins and cells.[41] It has frequently been reported that the hydrophilic modification of the PCL surfaces enhanced the early cell adhesion.[42,43] This improved initial cell adhesion event will affect subsequent cell proliferation, differentiation, and matrix production for cellular mineralization. Along with the improved hydrophilicity, the magnetism-related stimulation of cell behaviors should also be importantly considered. Several studies have also reported the influential role of MNPs incorporated within biomaterials and scaffolds in the cell proliferation and osteoblastic differentiation *in vitro*.[44,45] The MNPs were suggested to be a sort of single magnetic domain on the nanoscale, leading to significant alterations in ion channels of cell membrane that might be influential on the cell proliferation and differentiation behaviors.[46,47] The nanoscale-generated magnetism-effect can be strengthened with increasing the content of MNPs, which would have stronger effects on the in vitro outcomes.

3.5. In vivo tissue compatibility of magnetic scaffolds

In vivo tissue responses of the scaffolds were evaluated after subcutaneous implantation in the dorsal region of rats for 2 weeks, as a preliminary study on the tissue compatibility of the magnetic scaffolds. The recovery from the anesthesia was uneventful after surgery, and all animals showed normal healing process without material-related complications and remained in good health during the study period. At 2 weeks after surgery, the harvested samples surrounding the tissues did not show any macroscopic redness or inflammatory signs. The histological photographs of samples are shown in **Fig. 12**, and the microscopic tissue responses including the intensity of fibrous capsule formation, inflammatory response, capillary formation, and a granulation tissue rich in fibroblast, are scored in **Table 2**. No significant differences were observed between the three scaffold groups. Mild to moderate fibroblastic and angioblastic proliferation was observed in all the samples. Fibrous tissue encapsulation was shown in the scaffolds, which were minimally degraded. All of the scaffolds were filled with fibroblasts. While mild inflammatory response occurred in only a small part around the samples, overall no rejection reactions were found after implantation in the animals. The newly formed tissue showed good integration to the adjacent tissues in all the groups. Organized fibrous granulation tissue formed spaces between the scaffold and adjacent connective tissue and muscle. Fibroblasts existed within the adjacent fibrous capsules around these scaffold systems.

Collectively, the PCL-MNP magnetic scaffolds showed excellent tissue compatibility in rat subcutaneous model for 2 weeks, and the information delivers a minimal guideline of the possible use of the developed scaffolds for further biomedical applications. Therefore, more in-depth *in vivo* studies using bone regeneration models for longer implantation periods are needed to elucidate the efficacy of the magnetic scaffolds. While this issue remains as further study, the results on *in vitro* cellular responses to the scaffolds in the initial adhesion, proliferation and mineralization, as well as the favorable physic-chemical properties including high water affinity and swelling behavior, and improved mechanical properties support the usefulness of the magnetic scaffolds for the bone repair and regeneration.

4. Conclusion

The surface-functionalized MNPs incorporated within PCL at small contents (up to 10 wt.%) significantly improved the hydrophilicity and mechanical properties, while enabling superparamagnetic behaviors of the scaffolds. The PCL-MNP scaffolds were shown to promote apatite forming ability and stimulate cellular adhesion and mineralization while exhibiting good tissue compatibility. Although more in-depth studies on bone targeted efficacy are needed, the results demonstrated that the PCL-MNP magnetic scaffolds hold great promise for use in bone tissue engineering.

Acknowledgements

This work was supported by a grant of Priority Research Centers Program (grant #2009-0093829), through the National Research Foundation of Korea (NRF), Republic of Korea.

References

1. A. Amirfazli, *Nat. Nanotechnol.*, 2007, **2**, 467-468.
2. M. Arruebo, R. Fernández-Pacheco, M. R. Ibarra and J. Santamaría, *Nano today*, 2007, **2**, 22-32.
3. A. Ito, Y. Takizawa, H. Honda, K. Hata, H. Kagami, M. Ueda and T. Kobayashi, *Tissue Eng.*, 2004, **10**, 833-840.
4. R. A. Pérez, J.-E. Won, J. C. Knowles and H.-W. Kim, *Adv. Drug Del. Rev.*, 2013, **65**, 471-496.
5. S. Yang, K.-F. Leong, Z. Du and C.-K. Chua, *Tissue Eng.*, 2001, **7**, 679-689.
6. J.-H. Jang, O. Castano and H.-W. Kim, *Adv. Drug Del. Rev.*, 2009, **61**, 1065-1083.
7. M. Banobre-Lopez, Y. Pineiro-Redondo, R. De Santis, A. Gloria, L. Ambrosio, A. Tampieri, V. Dediu and J. Rivas, *J. Appl. Phys.*, 2011, **109**, 07B313-307B313-313.
8. A. Gloria, T. Russo, U. D'Amora, S. Zeppetelli, T. D'Alessandro, M. Sandri, M. Bañobre-López, Y. Piñeiro-Redondo, M. Uhlarz and A. Tampieri, *J. R. Soc. Interface*, 2013, **10**.
9. S. Sun, H. Zeng, D. B. Robinson, S. Raoux, P. M. Rice, S. X. Wang and G. Li, *J. Am. Chem. Soc.*, 2004, **126**, 273-279.
10. S.-J. Hong, H.-S. Yu, K.-T. Noh, S.-A. Oh and H.-W. Kim, *J. Biomater. Appl.*, 2010, **24**, 733-750.
11. L. Wu, H. Zhang, J. Zhang and J. Ding, *Tissue Eng.*, 2005, **11**, 1105-1114.
12. U. S. Shin, I.-K. Yoon, G.-S. Lee, W.-C. Jang, J. C. Knowles and H.-W. Kim, *J. Tissue Eng.*, 2011, **2**, 674287.
13. L. Withanawasam, A. Murphy, G. Hadjipanayis and R. Krause, *J. Appl. Phys.*, 1994, **76**, 7065-7067.
14. R. A. Perez, M. Kim, T.-H. Kim, J.-H. Kim, J. H. Lee, J.-H. Park, J. C. Knowles and H.-W. Kim, *Tissue Eng. A*, 2013.
15. P. Tartaj, M. del Puerto Morales, S. Veintemillas-Verdaguer, T. González-Carreno and C. J. Serna, *J. Phys. D: Appl. Phys.*, 2003, **36**, R182-R197.
16. S. L. Pinho, S. Laurent, J. Rocha, A. Roch, M.-H. Delville, S. Mornet, L. D. Carlos, L. Vander Elst, R. N. Muller and C. F. Geraldes, *J. Phys. Chem. C*, 2012, **116**, 2285-2291.
17. S. Sun and H. Zeng, *J. Am. Chem. Soc.*, 2002, **124**, 8204-8205.

18. Y. Wu, W. Jiang, X. Wen, B. He, X. Zeng, G. Wang and Z. Gu, *Biomed. Mater.*, 2010, **5**, 015001.

19. F. Yang, L. Li, Y. Li, Z. Chen, J. Wu and N. Gu, *Phys. Med. Biol.*, 2008, **53**, 6129-6141.

20. D. W. Hutmacher, T. Schantz, I. Zein, K. W. Ng, S. H. Teoh and K. C. Tan, *J. Biomed. Mater. Res.*, 2001, **55**, 203-216.

21. W. J. Li, C. T. Laurencin, E. J. Caterson, R. S. Tuan and F. K. Ko, *J. Biomed. Mater. Res.*, 2002, **60**, 613-621.

22. H. Yoshimoto, Y. Shin, H. Terai and J. Vacanti, *Biomaterials*, 2003, **24**, 2077-2082.

23. C. M. Murphy, M. G. Haugh and F. J. O'Brien, *Biomaterials*, 2010, **31**, 461-466.

24. R. R. Gil, B. Ruiz and M. S. Lozano, *J. Appl. Polym. Sci.*, 2013.

25. N. N. Fathima, A. Dhathathreyan and T. Ramasami, *Colloids Surf. B. Biointerfaces*, 2007, **57**, 118-123.

26. B. Zhang, Z. Tu, F. Zhao and J. Wang, *Appl. Surf. Sci.*, 2013, **266**, 375-379.

27. H. Borchert, E. V. Shevchenko, A. Robert, I. Mekis, A. Kornowski, G. Grübel and H. Weller, *Langmuir*, 2005, **21**, 1931-1936.

28. A. Nan, R. Turcu, I. Craciunescu, O. Pana, H. Scharf and J. Liebscher, *J. Polym. Sci., Part A: Polym. Chem.*, 2009, **47**, 5397-5404.

29. W. Yuan, J. Yuan, L. Zhou, S. Wu and X. Hong, *Polymer*, 2010, **51**, 2540-2547.

30. N. V. Jadhav, A. I. Prasad, A. Kumar, R. Mishra, S. Dhara, K. Babu, C. Prajapat, N. Mishra, R. Ningthoujam and B. Pandey, *Colloids Surf. B. Biointerfaces*, 2013, **108**, 158-168.

31. M. Tanahashi and T. Matsuda, *J. Biomed. Mater. Res.*, 1997, **34**, 305-315.

32. P. De la Presa, Y. Luengo, M. Multigner, R. Costo, M. Morales, G. Rivero and A. Hernando, *J. Phys. Chem. C*, 2012, **116**, 25602-25610.

33. A. Ito, K. Ino, M. Hayashida, T. Kobayashi, H. Matsunuma, H. Kagami, M. Ueda and H. Honda, *Tissue Eng.*, 2005, **11**, 1553-1561.

34. A. Tampieri, E. Landi, F. Valentini, M. Sandri, T. D'Alessandro, V. Dediu and M. Marcacci, *Nanotechnology*, 2011, **22**, 015104.

35. Y. Wu, W. Jiang, X. Wen, B. He, X. Zeng, G. Wang and Z. Gu, *Biomed. Mater.*, 2010, **5**, 1-7.

36. A. Figuerola, R. Di Corato, L. Manna and T. Pellegrino, *Pharmacol. Res.*, 2010, **62**, 126-143.

37. R. M. Erb, H. S. Son, B. Samanta, V. M. Rotello and B. B. Yellen, *Nature*, 2009, **457**, 999-

1002.

38. D. Barbieri, J. D. de Bruijn, X. Luo, S. Fare, D. W. Grijpma and H. Yuan, *J. Mech. Behav. Biomed.*, 2013, **20**, 162-172.

39. L. C. Wu, J. Yang and J. Kopeček, *Biomaterials*, 2011, **32**, 5341-5353.

40. M. P. Prabhakaran, J. Venugopal and S. Ramakrishna, *Acta Biomater.*, 2009, **5**, 2884-2893.

41. K. Tuzlakoglu, I. Pashkuleva, M. T. Rodrigues, M. E. Gomes, G. H. van Lenthe, R. Müller and R. Reis, *J. Biomed. Mater. Res. A*, 2010, **92**, 369-377.

42. H. C. Lai, L. F. Zhuang, X. Liu, M. Wieland, Z. Y. Zhang and Z. Y. Zhang, *J. Biomed. Mater. Res. A*, 2010, **93**, 289-296.

43. X. Bulliard, S. G. Ihn, S. Yun, Y. Kim, D. Choi, J. Y. Choi, M. Kim, M. Sim, J. H. Park and W. Choi, *Adv. Funct. Mater.*, 2010, **20**, 4381-4387.

44. S. Panseri, C. Cunha, T. D'Alessandro, M. Sandri, A. Russo, et al, *PLoS One,* 2012, **7(6)**, e38710.

45. Z. W. Gu, Y. Wu, W. Jiang, X. T. Wen, B. He, et al, *Biomed. Mater.,* 2010, **5**, 015001.

46. S. Hughes, A. J. El Haj, J. Dobson, *Med. Eng. Phys.*, 2005, **27(9)**, 754–762.

47. D. M. Huang, J. K. Hsiao, Y. C. Chen, L. Y. Chien, M. Yao, et al, *Biomaterials*, 2009, **30(22)**, 3645–3651

List of Tables and Figures

Table 1. Porosity and density of the scaffolds analyzed by mercury intrusion porosimetry, and the surface area measured by BET.

Table 2. Histopathologic assessments of the tissue responses in the scaffolds at 2 weeks after implantation in rat subcutaneous tissue. Four samples were implanted for each group, and the implanted samples were rated according to the cell numbers/intensity of the lesions; 0: not observed or very low numbers of infiltrated inflammatory cells, 1: mild changes or low numbers of infiltrated inflammatory cells, 2: moderate changes or intermediate numbers of infiltrated inflammatory cells, 3: severe changes/numbers of infiltrated inflammatory cells. FC: fibrous capsule, IR: inflammatory response, BV: blood vessel, FB: fibroblasts.

Fig. 1. Characteristics of surface-functionalized MNPs; (a) TEM and (b) hysteresis loop.

Fig. 2. SEM morphologies of PCL, PCL-MNP5, and PCL-MNP10 scaffolds showing a highly porous structure, and their EDS mapping images representing MNP (Fe) distribution in the scaffold.

Fig. 3. Characteristics of the scaffolds; (a) XRD pattern, (b) FT-IR spectrum, and (c) TG analysis of PCL, PCL-MNP5, and PCL-MNP10 scaffolds.

Fig. 4. (a) Water contact angle, (b) water uptake capacity, and (c) swollen volume of PCL, PCL-MNP5, and PCL-MNP10 scaffolds.

Fig. 5. Time- and MNP-dependent apatite-forming ability of the scaffolds; (a) SEM morphology and (b) XRD pattern of PCL, PCL-MNP5, and PCL-MNP10 scaffolds with SBF immersion for 1, 3, and 7 days. Scale bar is 5 μm in SEM images. Star-marked diffraction peaks at $2\theta \approx 26^\circ$ and 32° represent apatite-characteristic bands in XRD.

Fig. 6. (a) Field-dependent magnetization curves of PCL, PCL-MNP5, and PCL-MNP10 scaffolds measured at room temperature, and (b) magnetic distances between a permanent magnet and these magnetized scaffolds under a static magnetic field. Pictures show magnetic interactions of the scaffolds with a permanent magnet.

Fig. 7. Static mechanical properties of PCL, PCL-MNP5, and PCL-MNP10 scaffolds analyzed by (a) typical compressive stress-strain curves and (b) elastic moduli obtained from initial linear regions shown in inset of (a).

Fig. 8. Dynamic mechanical analyses of storage modulus (E’), loss modulus (E’’), tangent delta (E’’/E’), and their average values recorded in PCL, PCL-MNP5, and PCL-MNP10 scaffolds performed over a frequency sweep.

Fig. 9. Cell adhesion on the scaffolds for 1, 3, and 24 h; (a) SEM cell morphology and (b) CCK-kit assay. Scale bar is 50 μm in SEM micrographs. *$p < 0.05$ and **$p < 0.01$, by a one-way ANOVA test.

Fig. 10. Osteoblastic cell proliferation on the scaffolds; (a) SEM observation at a 14-day culture and (b) CCK-kit assay of the cells at 3-, 7-, 14-, and 21-day culture. *$p < 0.05$ and **$p < 0.01$, by a one-way ANOVA test.

Fig. 11. Cellular mineralization assay, by (a) ARS quantitative measurement of calcium deposits at 7-, 14-, and 21-day cultures, (b) EDS mapping of Ca (green) and P (blue) element deposited on cells cultured on PCL-MNP10 scaffolds during 21 days, and EDS spectra of Ca and P signals. *$p < 0.05$ and **$p < 0.01$, by a one-way ANOVA test.

Fig. 12. Histological stains of the implanted scaffolds for 2 weeks in rat subcutaneous tissue. All groups show similar regenerative patterns of thin capsule with mild inflammatory responses around scaffolds. The biological host response against the groups was minimal. F: Fibrous capsule, P: polymer, and R: residual MNP particles

Table 1

	porosimetry with mercury			BET with N_2 gas
	Porosity (%)	Skeletal Density (g/cm^3)	Bulk Density (g/cm^3)	Surface area(m^2/g)
PCL	64.5 ± 3.54	0.104 ± 0.0006	0.0364 ± 0.003	5.67 ± 1.32
PCL-MNP5	74.58 ± 1.95	0.248 ± 0.030	0.0551 ± 0.007	4.76 ±2.15
PCL-MNP10	70.9 ± 9.75	0.3705 ± 0.304	0.0620 ± 0.011	7.86 ± 0.44

Table 2

	PCL				PCL-MNP5				PCL-MNP10			
	FC	IR	BV	FB	FC	IR	BV	FB	FC	IR	BV	FB
# 1	1	1	1	2	1	1	1	2	1	1	1	2
# 2	1	1	1	2	1	1	1	2	1	2	1	2
# 3	2	2	1	2	1	2	1	2	2	1	1	2
# 4	2	1	1	2	1	2	1	2	2	1	1	2

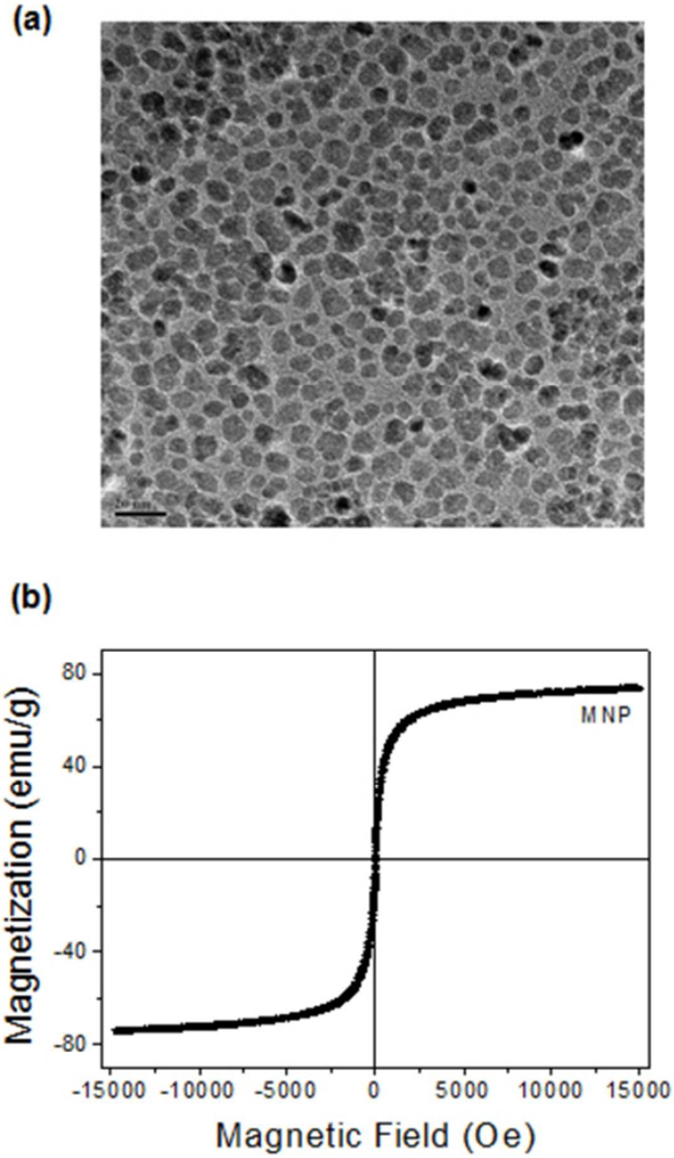

Fig. 1. Characteristics of surface-functionalized MNPs; (a) TEM and (b) hysteresis loop.
18x30mm (600 x 600 DPI)

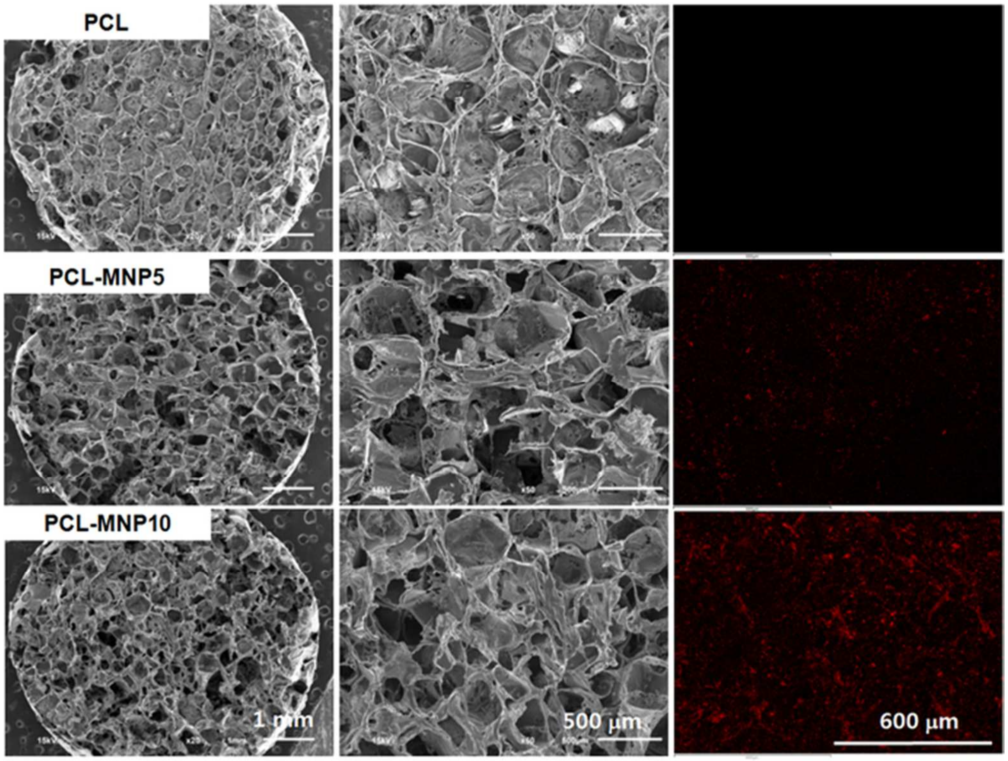

Fig. 2. SEM morphologies of PCL, PCL-MNP5, and PCL-MNP10 scaffolds showing a highly porous structure, and their EDS mapping images representing MNP (Fe) distribution in the scaffold.
29x22mm (600 x 600 DPI)

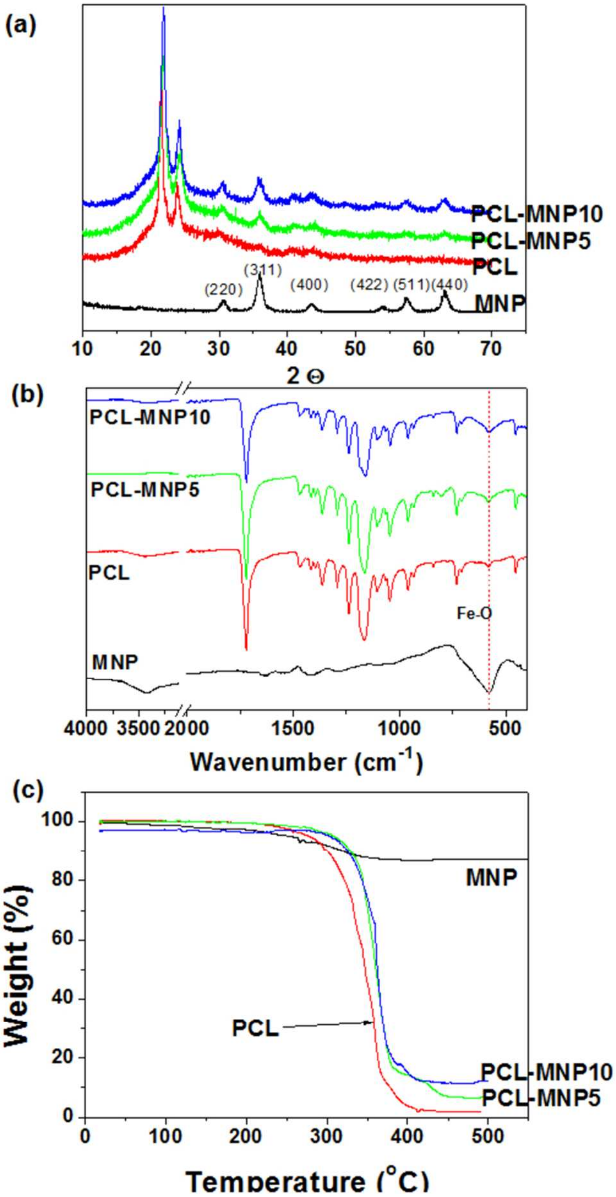

Fig. 3. Characteristics of the scaffolds; (a) XRD pattern, (b) FT-IR spectrum, and (c) TG analysis of PCL, PCL-MNP5, and PCL-MNP10 scaffolds.
31x59mm (600 x 600 DPI)

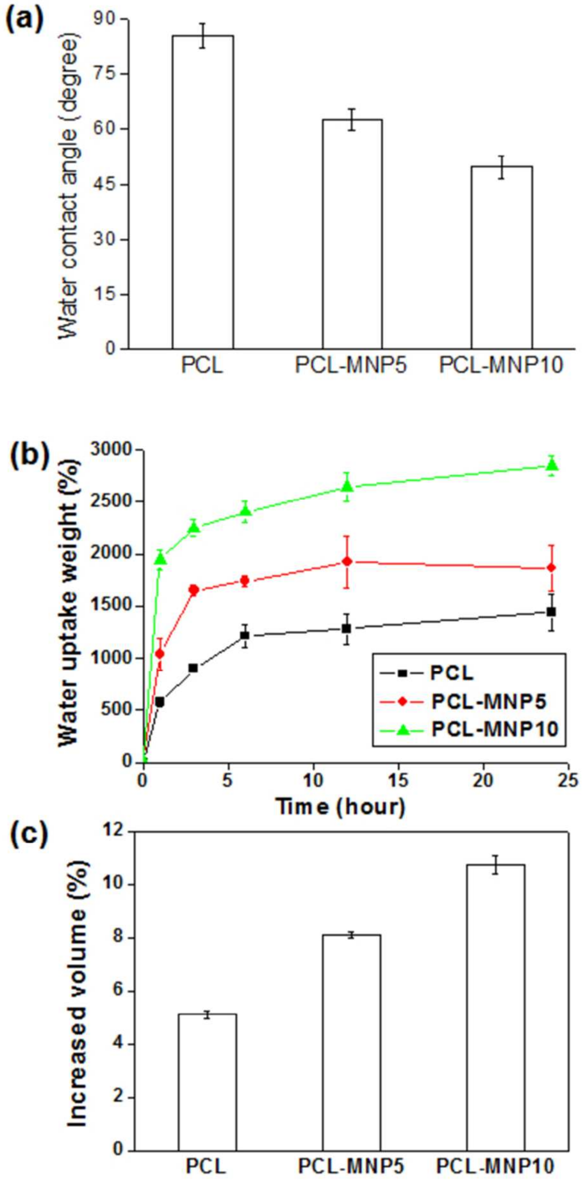

Fig. 4. (a) Water contact angle, (b) water uptake capacity, and (c) swollen volume of PCL, PCL-MNP5, and PCL-MNP10 scaffolds.
25x50mm (600 x 600 DPI)

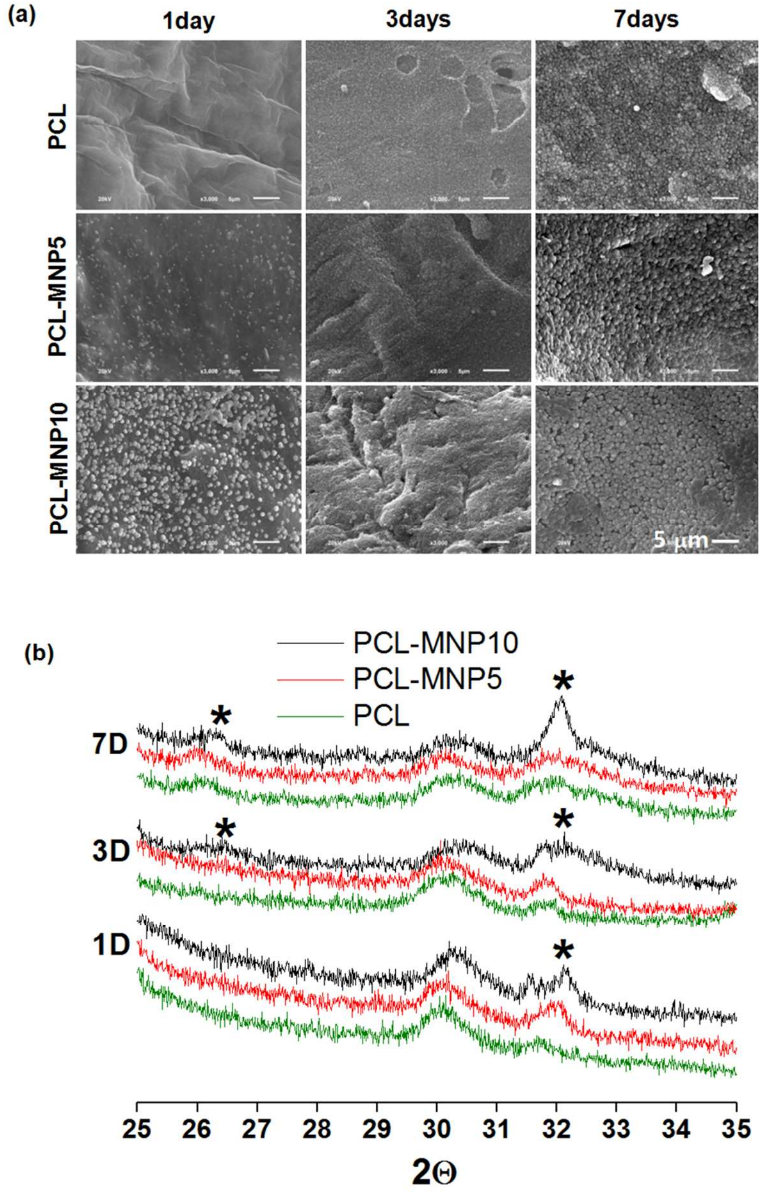

Fig. 5. Time- and MNP-dependent apatite-forming ability of the scaffolds; (a) SEM morphology and (b) XRD pattern of PCL, PCL-MNP5, and PCL-MNP10 scaffolds with SBF immersion for 1, 3, and 7 days. Scale bar is 5 μm in SEM images. Star-marked diffraction peaks at 2θ ≈ 26º and 32º represent apatite-characteristic bands in XRD.
43x68mm (600 x 600 DPI)

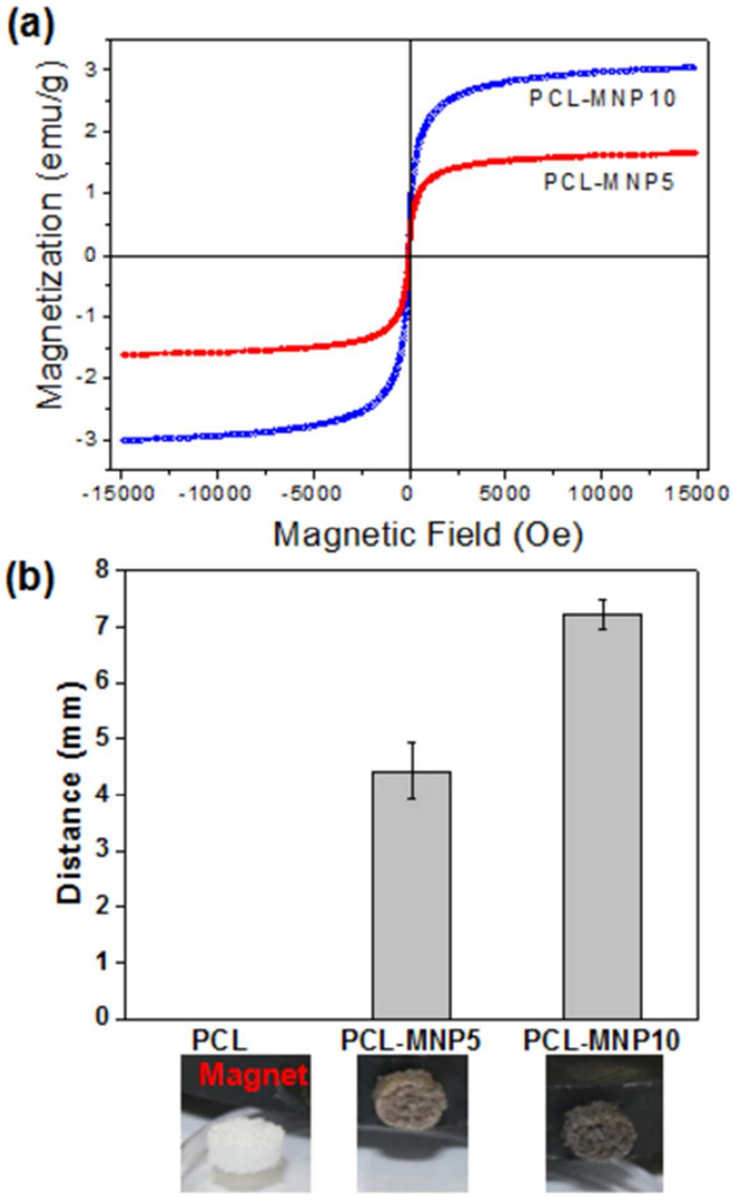

Fig. 6. (a) Field-dependent magnetization curves of PCL, PCL-MNP5, and PCL-MNP10 scaffolds measured at room temperature, and (b) magnetic distances between a permanent magnet and these magnetized scaffolds under a static magnetic field. Pictures show magnetic interactions of the scaffolds with a permanent magnet.
18x29mm (600 x 600 DPI)

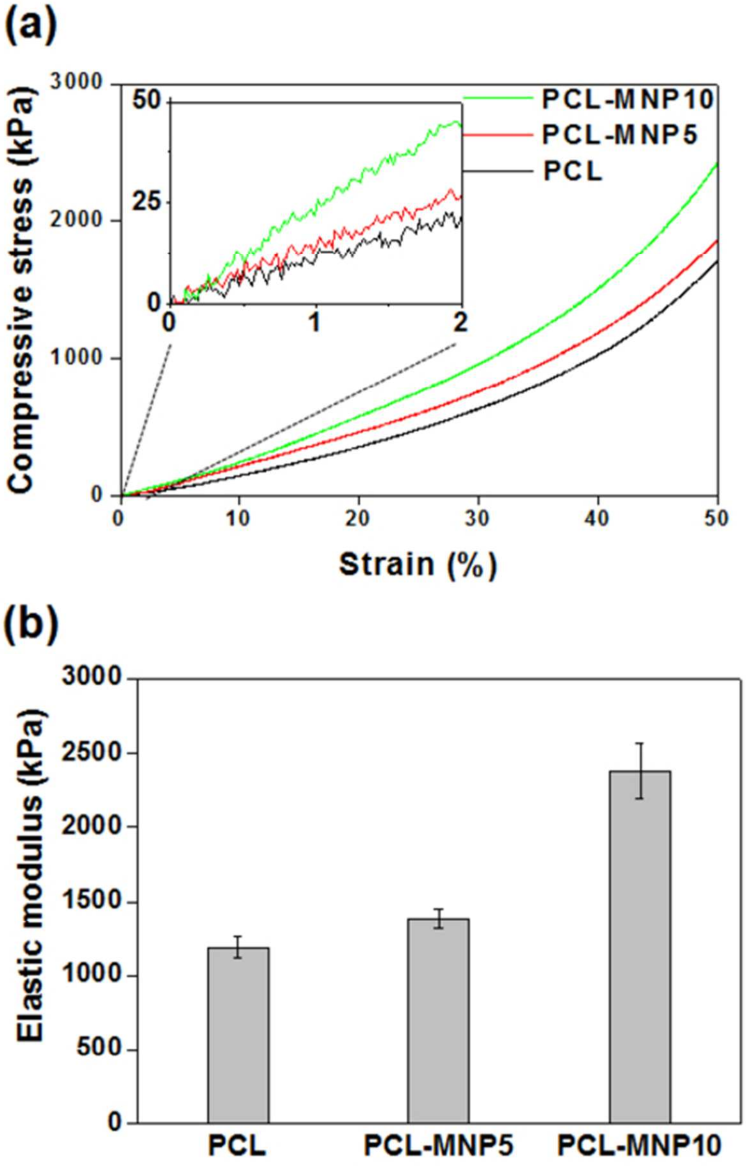

Fig. 7. Static mechanical properties of PCL, PCL-MNP5, and PCL-MNP10 scaffolds analyzed by (a) typical compressive stress-strain curves and (b) elastic moduli obtained from initial linear regions shown in inset of (a).
23x34mm (600 x 600 DPI)

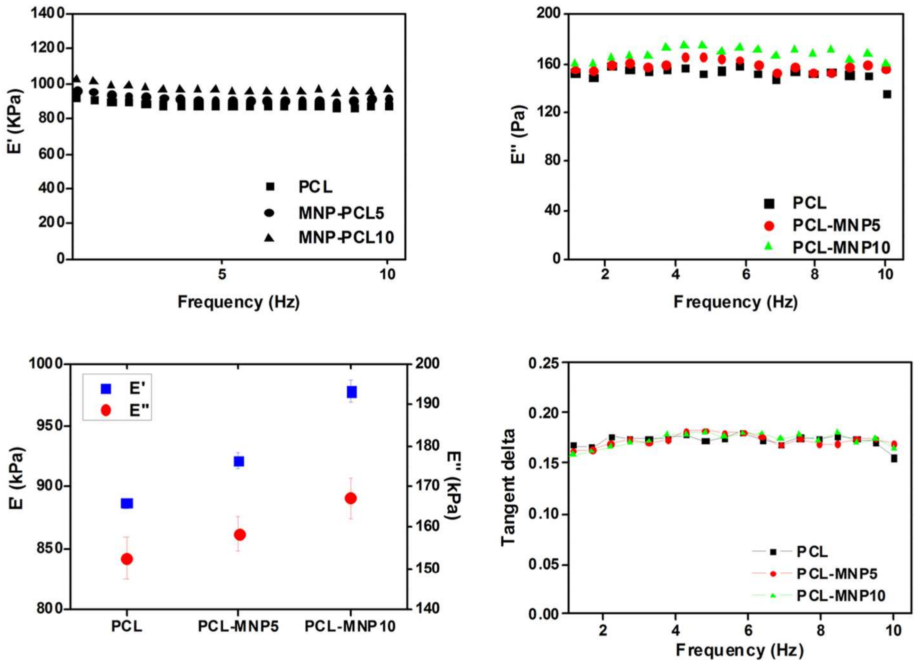

Fig. 8. Dynamic mechanical analyses of storage modulus (E'), loss modulus (E''), tangent delta (E''/E'), and their average values recorded in PCL, PCL-MNP5, and PCL-MNP10 scaffolds performed over a frequency sweep.
122x85mm (300 x 300 DPI)

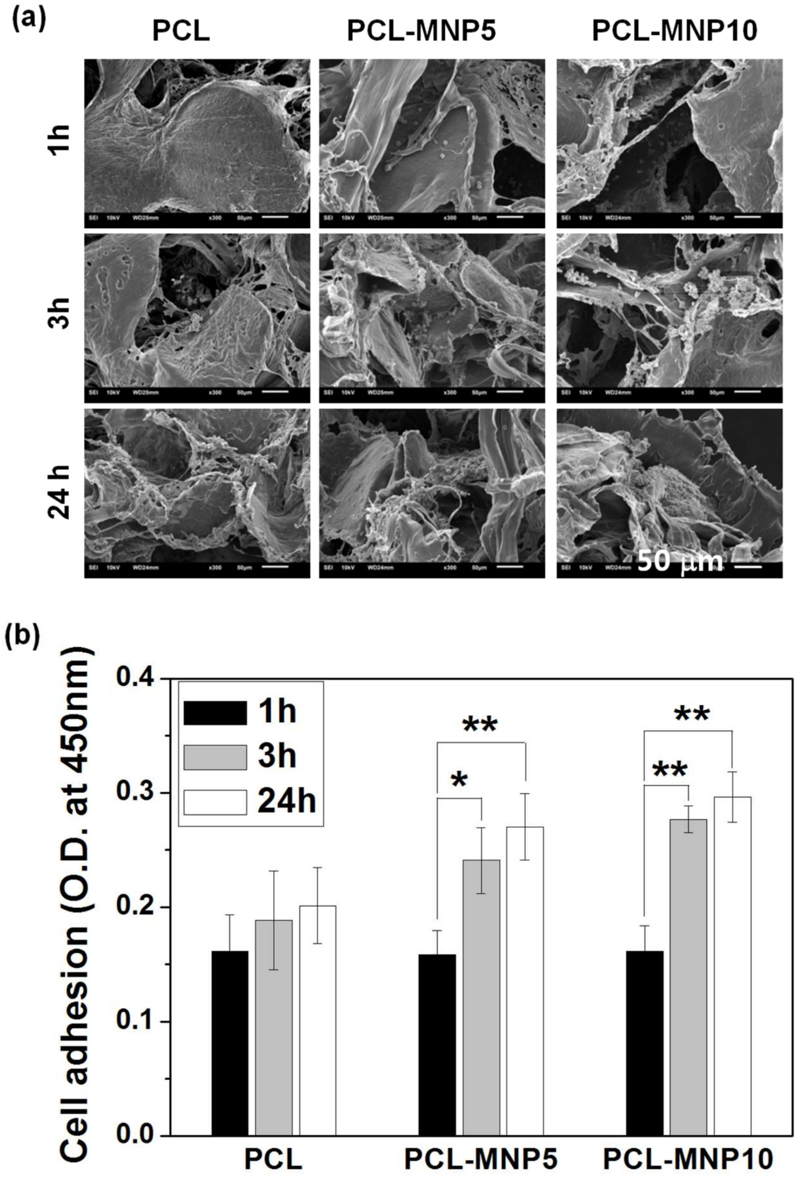

Fig. 9. Cell adhesion on the scaffolds for 1, 3, and 24 h; (a) SEM cell morphology and (b) CCK-kit assay. Scale bar is 50 μm in SEM micrographs. $^*p < 0.05$ and $^{**}p < 0.01$, by a one-way ANOVA test.
55x82mm (600 x 600 DPI)

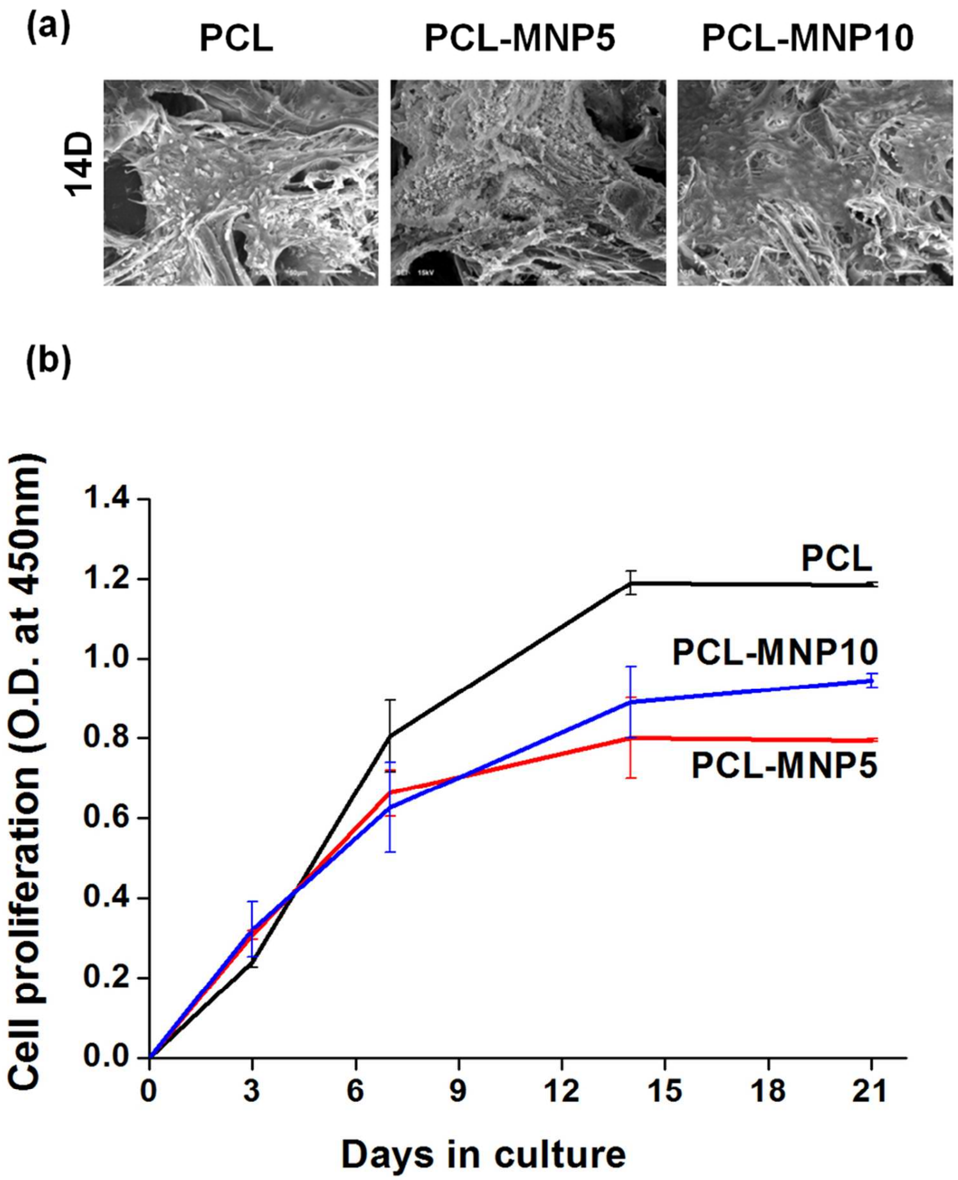

Fig. 10. Osteoblastic cell proliferation on the scaffolds; (a) SEM observation at a 14-day culture and (b) CCK-kit assay of the cells at 3-, 7-, 14-, and 21-day culture. *$p < 0.05$ and **$p < 0.01$, by a one-way ANOVA test.
43x52mm (600 x 600 DPI)

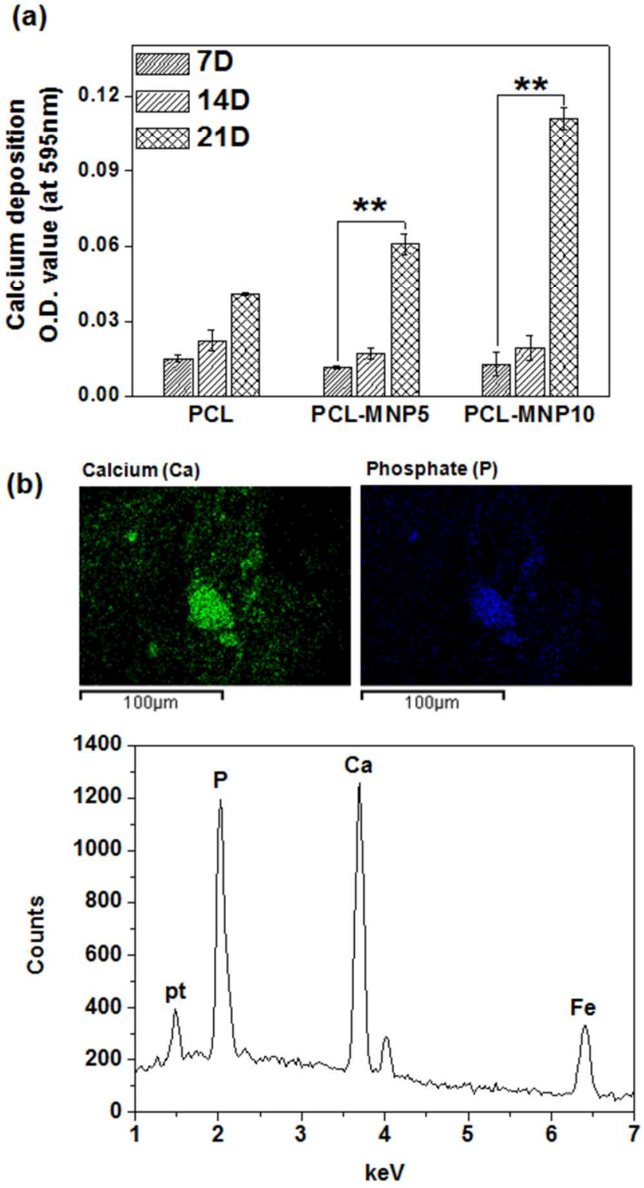

Fig. 11. Cellular mineralization assay, by (a) ARS quantitative measurement of calcium deposits at 7-, 14-, and 21-day cultures, (b) EDS mapping of Ca (green) and P (blue) element deposited on cells cultured on PCL-MNP10 scaffolds during 21 days, and EDS spectra of Ca and P signals. $*p < 0.05$ and $**p < 0.01$, by a one-way ANOVA test.
27x49mm (600 x 600 DPI)

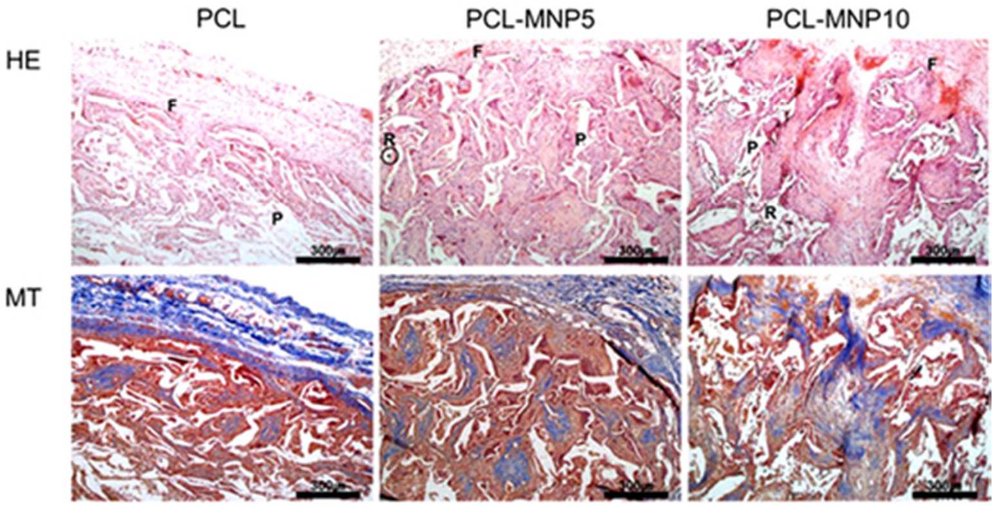

Fig. 12. Histological stains of the implanted scaffolds for 2 weeks in rat subcutaneous tissue. All groups show similar regenerative patterns of thin capsule with mild inflammatory responses around scaffolds. The biological host response against the groups was minimal. F: Fibrous capsule, P: polymer, and R: residual MNP particles
22x11mm (600 x 600 DPI)